An Eulerian-based finite element approach for simulating cone-penetration tests in soft clay

A. S. Osman
Durham University, Durham, United Kingdom, ashraf.osman@durham.ac.uk

ABSTRACT: In the numerical simulations of full-flow (T-bar and ball) penetrometers and cone penetration test, the onset and growth of damage in the surrounding geomaterial depend on the rates of deformation and the magnitude of strain (or material structure). In such applications, modelling the deformation and stress histories of soil particles as they move during the penetration process is important. This paper presents a novel Eulerian-based finite element formulation to study the effect of strain softening on penetrometers resistance. The novelty of this approach is that it is capable of simulating large deformations without the need for re-meshing. The gradient of the stress at each Gaussian point is calculated using a smoothing thin-plate splines (TPS) technique. This novel approach has been used to simulate T-bar and cone-penetration tests in soft clay. The results show that the effect of softening is much less significant for the cone penetration test compared to T-bar penetration.

Keywords: clays; Eulerian finite element analysis; penetrometers.

1. Introduction

The cone penetration test is one of the most widely in-situ tests in geotechnical engineering practice for assessing the strength profile in soil. In saturated clay, the test is performed at a penetration rate that does not permit drainage during the penetration process, so the test may be interpreted directly as a measure of the undrained strength profile of the clay. The popularity of this in situ testing device has resulted in great demand for the development of accurate correlations between measured cone quantities (e.g., cone resistance and sleeve friction ratio) and engineering properties of the soil. Despite extensive research on cone penetration test in the last two decades [1-7] the effect of strain-softening on the cone resistance has not been investigated in detail.

In the numerical simulation of the cone penetration test (CPT) and full-flow penetrometers such as T-bar and ball tests, modelling the deformation and stress histories of soil particles as they move during the penetration process is important. Soils tend to exhibit a drop in strength after significant shearing. This strain softening behaviour can be related both to the reorientation of platy clay minerals during large strains, and to the "critical state" strength degradation in over-consolidated clays [8]. Randolph [9] has illustrated that the undrained shear strength is exponentially decayed with the cumulative shear strain.

The finite element method has been implemented successfully to model history-dependent geotechnical problems [10]. The formulations are based either on small deformations (which is not suitable for large-strain problems such as CPT) or using Lagrangian theory. Finite element discretisations with Lagrangian meshes are commonly classified as updated Lagrangian formulations and total Lagrangian formulations. Both formulations use Lagrangian descriptions, i.e. the dependent variables are functions of the material (Lagrangian) coordinates and time. In the updated Lagrangian formulation, the derivatives are with respect to the spatial (Eulerian) coordinates; the weak form involves integrals over the deformed (or current) configuration. In the total Lagrangian formulation, the weak form involves integrals over the initial (reference) configuration and derivatives are taken with respect to the material coordinates.

2. Finite element

2.1. Formulation

The principal of virtual work in the Total Lagrangian can be written as:

$$\int_{\Omega_0} \delta F_{ij} P_{ji} d\Omega_0 - \int_{\Omega_0} \delta u_i \rho_0 b_i d\Omega_0 - \int_{\Gamma_0} \delta u_i \bar{t}_i d\Gamma_0 + \int_{\Omega_0} \delta u_i \rho_0 \ddot{u}_i d\Omega_0 = 0 \quad (1)$$

where Ω_0 is the domain of the undeformed configuration, Γ_0 is the boundary of that domain, u_i is the displacement, ρ_0 is the mass density in the undeformed domain, b_i is the body forces, $\bar{t}_i$ is the traction force, P_{ij} are the nominal stresses and F_{ij} is the deformation gradient given by:

$$F_{ij} = \frac{\partial x_i}{\partial X_j} \quad (2)$$

where X_i is the material (Lagrangian) coordinates and x_i is the spatial (Eulerian) coordinate (see Fig. 1).

The equation of motion (the discrete momentum equation) can be derived by:

$$M_{ijIJ} \ddot{u}_{jJ} + f_{iI}^{\text{int}} = f_{iI}^{ext} \quad (3)$$

where f_{iI}^{int} are the internal nodal forces given by:

$$f_{iI}^{\text{int}} = \int_{\Omega_0} \frac{\partial N_I}{\partial X_j} P_{ji} d\Omega_0 \tag{4}$$

$N_I(X)$ is the shape function and f_{iI}^{ext} are the external nodal forces given by:

$$f_{iI}^{ext} = \int_{\Omega_0} N_I \rho_0 b_i d\Omega_0 + \int_{\Gamma_0} N_I \bar{t}_i d\Gamma_0 \tag{5}$$

and the mass matrix in the Total Lagrangian is given by:

$$M_{ijIJ} = \delta_{ij} \int_{\Omega_0} \rho_0 N_I N_J d\Omega_0 \tag{6}$$

The nominal stresses P_{ij} are related to the Second Piola-Kirchhoff (PK2) stresses S_{ij} by:

$$P_{ij} = S_{ir} F_{rj}^T \tag{7}$$

Taking the time derivative of the internal nodal forces is therefore gives:

$$\dot{f}_{iI}^{\text{int}} = \int_{\Omega_0} \frac{\partial N_I}{\partial X_J} \dot{S}_{jr} F_{ir} d\Omega_0 + \int_{\Omega_0} \frac{\partial N_I}{\partial X_J} S_{jr} \dot{F}_{ir} d\Omega_0 \tag{8}$$

Eq. 8 shows that the rate of the internal nodal forces consists of two distinct parts:

1. The first term depends on the material response (the rate of stress $\dot{\mathbf{S}}$) and leads to what is called the material tangent stiffness matrix **K***mat* .
2. The second term accounts for rotation of the stress with the motion. This term is called the geometric stiffness. It is denoted by **K***geo* .

The rate of stress $\dot{\mathbf{S}}$ can be related to the rate of Green strain $\dot{\mathbf{E}}$ using the tangent stiffness matrix **C**:

$$\dot{S}_{ij} = C_{ijkl}^{SE} \dot{E}_{kl} \tag{9}$$

The rate of Green strain $\dot{\mathbf{E}}$ can be related to the rate of nodal velocity $\dot{\mathbf{d}}$ by:

$$\left\{\dot{\mathbf{E}}\right\} = \mathbf{B_0} \left\{\dot{\mathbf{d}}\right\} \tag{10}$$

Eq. 7 can be converted to updated Lagrangian forms by letting the current configuration be a reference configuration (see Fig. 1). Therefore, Eq. 7 can be rewritten as:

$$\dot{\mathbf{f}}_{\mathbf{I}}^{\mathbf{int}} = \left(\int_{\Omega} \mathbf{B}_I^{\mathbf{T}} \left[\mathbf{C}^{\sigma T} \right] \mathbf{B}_J d\Omega + \mathbf{I} \int_{\Omega} \boldsymbol{\beta}_I^T \boldsymbol{\sigma} \boldsymbol{\beta}_J^T d\Omega \right) \dot{\mathbf{u}}_J \tag{11}$$

where

$$\beta_{iI} = \frac{\partial N_I}{\partial X_i} \tag{12}$$

Therefore, from Eq. (11), the material tangent stiffness can be defined as:

$$\mathbf{K}_{IJ}^{mat} = \int_{\Omega} \mathbf{B}_I^{\mathbf{T}} \left[\mathbf{C}^{\sigma T} \right] \mathbf{B}_J d\Omega \tag{13}$$

And the geometric stiffness matrix is given by:

$$\mathbf{K}_{IJ}^{geo} = \mathbf{I} \int_{\Omega} \boldsymbol{\beta}_I^T \boldsymbol{\sigma} \boldsymbol{\beta}_J^T d\Omega \tag{14}$$

In finite deformation analyses, an objective rate is needed in the definition of constitutive model to ensure that rigid body motions do not influence the stress state in the material. Several definitions of objective stress rates can be found in the literature (see [11] for example). A widely used stress rate that satisfying objectivity is the Jaumann rate:

$$\dot{\sigma}_{ij} = \sigma_{ij}^{\nabla J} - \sigma_{ik}\omega_{kj} + \omega_{ik}\sigma_{kj} \tag{15}$$

where $\dot{\sigma}_{ij}$ is the Cauchy stress rate, $\sigma_{ij}^{\nabla J}$ is the Jaumman objective stress rate and ω_{kj} is the spin tensor defined as:

$$\omega_{ij} = \frac{1}{2}\left(\frac{\partial v_i}{\partial x_j} - \frac{\partial v_j}{\partial x_i} \right) \tag{16}$$

where $\mathbf{v}$ is the velocity vector.

The material tangent moduli relating the Jaumman rate of Cauchy stress to the rate of deformation can be defined as:

$$\sigma_{ij}^{\nabla J} = C_{ijkl}^{\sigma J} D_{kl} \tag{17}$$

The Jaumann and the Trusdell tangent moduli can be related as follows (see [1])

$$\mathbf{C}^{\sigma T} = \mathbf{C}^{\sigma J} - \mathbf{C}^{*} \tag{18}$$

where

$$C_{ijkl}^{*} = \frac{1}{2}\left(\delta_{ik}\sigma_{ji} + \delta_{il}\sigma_{jk} + \delta_{jk}\sigma_{il} + \delta_{jl}\sigma_{ik} \right) - \sigma_{ij}\delta_{kl} \tag{18}$$

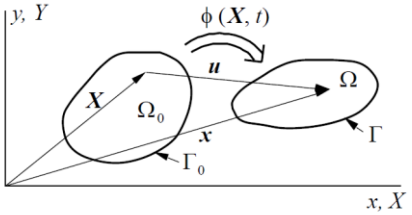

Fig. 1 FE configuration

Therefore the material tangent matrix for Jaumann rate can be rewritten as:

$$\mathbf{K}_{IJ}^{mat} = \int_{\Omega} \mathbf{B}_I^{\mathbf{T}} \left[\mathbf{C}^{\sigma J} - C^{*} \right] \mathbf{B}_J \, d\Omega \tag{19}$$

For more details on the mathematical derivation, the reader should refer to [11].

The material derivative $\dot{f}$ in the Eulerian frame of reference is described by:

$$\dot{f} = \frac{Df}{Dt} = \frac{\partial f}{\partial t} + v_i \frac{\partial f}{\partial x_i} \tag{20}$$

The stress state in a path-dependent material depends on the history of the material point. In the Eulerian description, the quadrature points do not coincide with the material points. Therefore, the stress history needs to be convected by the velocity. The material derivative of Cauchy stresses is given by:

$$\dot{\sigma}_{ij} = \frac{\partial \sigma_{ij}}{\partial t} + v_k \frac{\partial \sigma_{ij}}{\partial x_k} = \Lambda \tag{21}$$

where Λ is evaluated from the constitutive relations and the consistency condition. Considering the Jauma rate:

$$\Lambda = C_{ijkl}^{\sigma J} D_{kl} + \sigma_{kj} \omega_{ik} + \sigma_{ki} \omega_{jk} \tag{22}$$

The operator splitting technique [12] can be used to solve the above equation. Eq. 21 can be decomposed into sets of simple partial differential equation operators, which can be solved sequentially as follows:

$$\begin{aligned} \dot{\sigma}_{ij} &= \Lambda \\ \frac{\partial \sigma_{ij}}{\partial t} + v_k \frac{\partial \sigma_{ij}}{\partial x_k} &= 0 \end{aligned} \tag{23}$$

The first set can be solved without considering the convective effect. Thus it can be evaluated in the same manner as in an updated Lagrangian analysis.

2.2. Stress integration

For non-linear materials, the stress-strain relations are usually given in rate form and have to be solved by integration for a given strain increment. The integration of 29 over the time period from t to $t + \Delta t$ is given by:

$$\begin{aligned} \sigma_{ij}^{t+\Delta t} &= \sigma_{ij}^{t} + \int_{0}^{\Delta \varepsilon_{kl}} C_{ijkl}^{\sigma J} \, d\varepsilon_{kl} \\ &+ \int_{0}^{\Delta \Omega_{ik}} \left(\sigma_{kj} \Delta t d\Omega_{ik} + \sigma_{ki} d\Omega_{kl} \right) \end{aligned} \tag{24}$$

Where

$$\Omega_{ij} = \frac{1}{2} \left(\frac{\partial u_i}{\partial x_j} - \frac{\partial u_j}{\partial x_i} \right) \tag{25}$$

Hughes and Winget [13] considered the skew-symmetry of Ω_{ij} and shows that the second integration in Eq. 24 is equivalent to a stress transformation:

$$\sigma_{ij}^{t} + \int_{0}^{\Delta \Omega_{ik}} \left(\sigma_{kj} d\Omega_{ik} + \sigma_{ki} d\Omega_{kl} \right) = Q_{ik} \sigma_{kl}^{t} Q_{jl} \tag{26}$$

where

$$Q_{ij} = \frac{\left(\delta_{kj} + \frac{1}{2} \Delta \Omega_{kj} \right)}{\left(\delta_{ik} - \frac{1}{2} \Delta \Omega_{ik} \right)} \tag{27}$$

2.3. Calculation of stress gradient

The gradient of the stress at each Gaussian point is required for calculating the internal force rate vector (Eq. 21 combined with Eq. 23). Inaccuracies in the calculation of the stress gradient could lead to numerical instability problems. In order to calculate the stress gradient, the smoothing thin-plate splines (TPS) technique [14,15] is employed. Thin plate splines are a special case of the Polyharmonic splines and are very useful for interpolation of scattered data in two-dimensions. The construction is based on choosing a function that minimises an integral that represents the bending energy of a surface. The globally constructed spline has continuous second-order derivatives.

A thin-plate interpolation scheme is used for interpolating the stress and for calculating the stress gradient. In this scheme, a function $f(x)$ is chosen so that that exactly interpolates the data points (i.e. $y_i = f(x_i)$), and minimises the bending energy of the spline surface:

The problem can be formulated with a smoothing parameter for regularisation [15]. A function f is chosen that does not necessarily exactly interpolate all the data points but that does minimise:

$$E[f] = \sum_{i=1}^{m} \left| f(\mathbf{x}_i) - y_i \right|^2 + \alpha \int_{\Re^n} \left| D^2 f \right|^2 dX \tag{28}$$

where α the smoothing parameters, m is the number of the data points and D^2f is the matrix of second-order partial derivatives of f.

The solution Eq. 28 is a linear combination of Green's functions together with a linear polynomial term:

$$f(\mathbf{x}) = \sum_{i=1}^{m} \frac{y_i - f(x_i)}{\alpha} G(\mathbf{x}, \mathbf{x}_i) + \left(b_0 + \sum_{j=1}^{n} b_j x_j \right) = \sum_{i=1}^{m} w_i G(\mathbf{x}, \mathbf{x}_i) + \left(b_0 + \sum_{j=1}^{n} b_j x_j \right) \quad (29)$$

where G(x, s) is the Green's function and x_j is the jth component of the variable x which in 2D could take the form:

$$G(r) = r^2 \ln r \quad (30)$$

where $r = \|\mathbf{x} - \mathbf{x}_i\|$, and $\|\bullet\|$ denotes the usual Euclidean norm.

Evaluating Eq. (30) at data point k we obtain

$$y_k = \sum_{i=1}^{m} w_i G(\mathbf{x}_k, \mathbf{x}_i) + \left(b_0 + \sum_{j=1}^{n} b_j x_j^{(k)} \right) + \alpha w_k \quad (31)$$

where $x_j^{(k)}$ is the jth component of $\mathbf{x}_k$.

which can be rewritten in matrix form as:

$$\mathbf{y} = (\mathbf{M} + \alpha \mathbf{I})\mathbf{w} + \mathbf{N}\mathbf{b} \quad (32)$$

In order for $f(\mathbf{x})$ to have square-integrable second derivatives, the orthogonality condition needs to be satisfied [15].

$$\mathbf{N}^T \mathbf{w} = \mathbf{0} \quad (33)$$

Thus, the coefficients **w** and **b** can be obtained by solving the following system:

$$\begin{bmatrix} (\mathbf{M} + \alpha \mathbf{I}) & \mathbf{N} \\ \mathbf{N}^T & \mathbf{0} \end{bmatrix} \begin{Bmatrix} \mathbf{w} \\ \mathbf{b} \end{Bmatrix} = \begin{Bmatrix} \mathbf{y} \\ \mathbf{0} \end{Bmatrix} \quad (34)$$

For more details on the implementation of thin-plate splines, the reader is referred to [15].

The problem varies from the thin-plate spline interpolant to the data when the regularisation parameter α is 0 to the least-squares approximation to the data by a linear polynomial when $\alpha \to \infty$. In the FE results reported here the regularisation parameter, α is chosen in the ad hoc fashion adopted in MATLAB, where α is taken to be equal to the average of the diagonal element of the matrix $\mathbf{Q}^T\mathbf{M}\mathbf{Q}$, where **Q** is the orthogonal matrix in the QR decomposition of **N**.

The stress gradient calculations are carried out in element-by-element fashion. For each element, the Gaussian points in this element and in its neighbouring elements are used in the interpolation. For each stress component, a function that interpolates the stress in all the Gaussian points is found together with its derivatives. Fig. 2 illustrates the elements patch used in the thin-plate spline calculations. In order to calculate the stress gradient in the element shown in the dark grey, the stress points in the surrounding elements are also taken into consideration to obtain the coefficients **w** and **b** in Eq. 34.

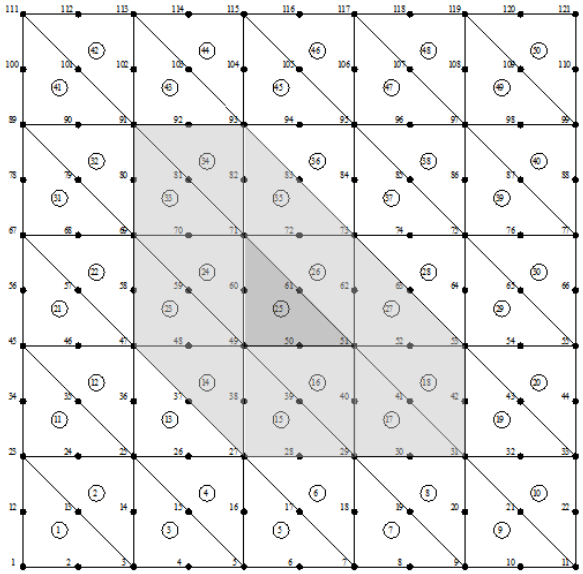

Fig. 2 Illustration of an element patch for the thin-plate spline interpolation

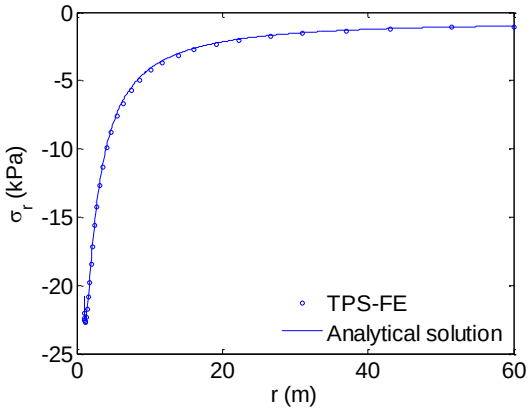

Fig. 3 Illustration of an element patch for the thin-plate spline interpolation

In order to demonstrate the efficiency of the thin plate spline technique, a Lagrangian finite element analysis has been carried out to calculate the stress gradient around a 1m diameter rigid T-bar embedded in an elastic medium which has a Young's modulus of 10000 kN/m^2 and Poisson's ratio of 0.49. The outer boundary is located at a radial distance of $60r_0$. A prescribed displacement of 0.01 m is applied to the outer boundary while the T-bar is taken to be stationary. Fig. 3 shows the radial stress along the centreline computed from the finite element using thin-plate splines compared with the closed-form solution of Bagulien et al. [16]. As it can be seen from there is an excellent agreement between the thin-plate spline interpolation and the closed-form solution.

2.4. FE model for CPT

Figure 4 shows the finite element mesh used in the analysis. The mesh consisted of 1701 nodes and 800 six noded reduced integration of triangular elements. The outer boundary was fixed in the radial direction. Displacement controlled analysis was performed, and the cone is taken to be stationary. A standard 60^o cone with a smooth interface between cone and soil was simulated. Soil movement normal to the cone-soil interface was prevented and only sliding motion allowed. It should be noted that applying this boundary condition at the tip of the cone will give a conservative estimate for the soil strength. Detailed discussion on boundary conditions of CPT can be found in [17]. The radial distance to the outer boundary was chosen to be well outside the plastic zone. Based on cavity expansion analysis [18] the ratio of plastic radius to the current cavity radius remains constant at $\sqrt{I_r}$ (where I_r is the rigidity index on the cone resistance defined as the ratio between the soil shear modulus G and the undrained shear strength s_u. $I_r=G/s_u$). The radial distance was taken to be 30R which is wide enough for the range of rigidity index between 50 and 500, which was investigated in the finite element simulations. Isotropic initial stress states were assumed. In all the analysis, a linear elastic model with von Mises failure criterion.

The von Mises yield stress (σ_y) is equivalent to twice the undrained shear strength of the soil s_u in triaxial compression test (i.e. $\sigma_y = 2s_u$).

Fig 5 shows that the rigidity index of the soil has a significant influence on the cone factor. Figure 5 compares the Eulerian-based finite element analysis with two finite element techniques: ALE and RITSS. In the Arbitary Lagrangian Eulerian (ALE) formulations, the mesh motion does not necessarily coincide with the material deformation so that severe element distortion can be eliminated. An effective algorithm for updating the mesh is needed since numerical errors may develop and propagate over time during the analysis. The implicit remeshing and interpolation technique by small strain (RITSS). RITSS could be regarded as a variant of the Aribitary Largranigian-Eulerian ALE method. However, the mesh topography and connectivity are not influenced by the previous deforming increment. These results illustrate that the current Eulerian analysis, enhanced with the thin-plate spline technique, gave results that are consistent with RITSS analysis of Lu et al. [19] and the ALE analysis of Nazem et al. [20].

2.4.1. Analysis of Cone Penetration Test in a strain-softening material

In strain-softening material, the strength of the soil can be expressed as a function of the cumulative plastic strain. Einav and Randolph [21] suggested a simple function of the form:

$$s_u = s_{u0}\left(\delta_{rem} + (1-\delta_{rem})e^{-3\lambda/\lambda_{ref}}\right) \quad (35)$$

where the ratio λ / λ_{ref} is the ratio of the measure of current accumulative plastic strain normalised by a reference value. Einav and Randolph [21] took the cumulative engineering shear strain λ (defined in equation (35)) as the measures of cumulative strain for a Tresca material, compared with the von Mises model adopted here. λ_{ref} is the cumulative shear strain required to cause 95% reduction (from peak value to remoulded). δ_{rem} represents the fully remoulded strength ratio (i.e. $s_{u(remolded)}/s_{u0}$) or the inverse of the sensitivity index, S_t.

It should be noted that the rate of penetration and therefore the strain rate increasing shear rate causes the soil to be stiffer [21]. However, for the sake of simplifaction and validation of the new technique, the rate-dependent response was not modelled in this work.

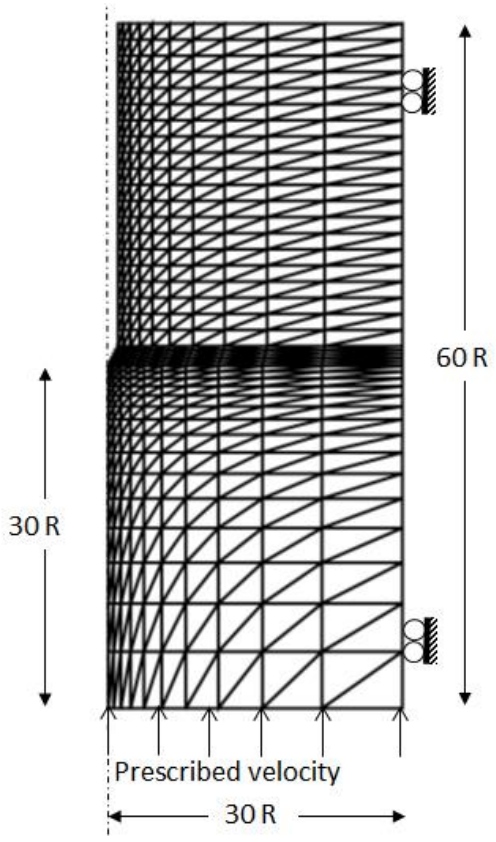

Fig. 4 Finite element mesh for CPT analysis

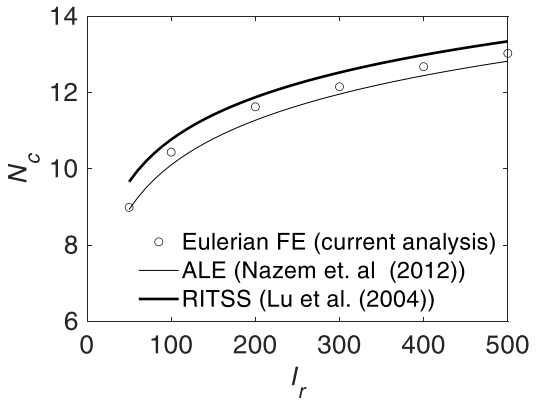

Fig. 5 Effect of rigidity index on the cone resistance

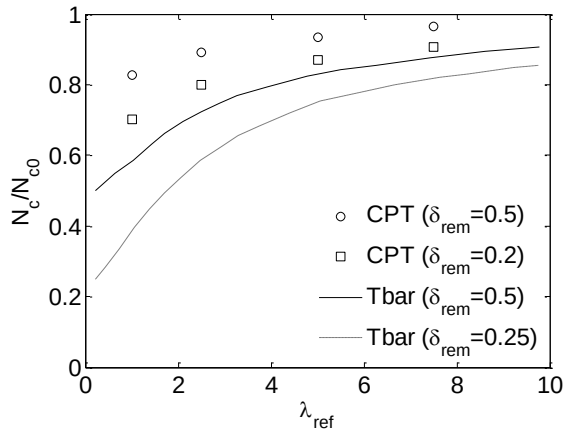

Fig. 6 Effect of strain softening on cone test: comparison between CPT and T-bar

Fig. 6 compares the effect of strain softening in the cone penetration test and in the T-bar as given by Eq. 32. The figure shows that the effect of softening in the CPT is much lower than for the T-bar. The reduction in cone-resistance is about 20 % of the reduction in T-bar resistance for the case of δ_{rem} = 0.5. More discussion on the effect of strain-softening on penetrometers can be found in [22]. The results in Fig. 6 were obtained using the constitutive model parameters shown in Table 1.

Table 1 Parameters used in the finite element analysis for CPT in a strain-softening material.

Paramter	Value
Young Modulus	10000 kN/m^2
Poisson's ratio	0.49
Initial undrained shear strength	25kPa
cumulative shear strain required to cause 95% reduction λ_{ref}	5.0

2.5. Conclusions

A novel Eulerian-based finite element formulation is developed to study the effect of strain softening on penetrometers resistance. The novelty of this approach is that it is capable of simulating large deformations without the need for re-meshing. The gradient of the stress at each Gaussian point is calculated using a smoothing thin-plate splines (TPS) technique. This approach gives consistent results and show that the effect of softening is much less significant for the cone penetration test compared to T-bar penetration. The reduction in cone resistance due to strain-softening is about 20 % of the reduction in T-bar resistance for the case of a sensitivity index of 2.

References

[1] Teh, C.I. & Houlsby, G.T; An analytical study of the cone penetration test in clay. Geotechnique 1991 41(1): 17-34.

[2] Whittle AJ. Constitutive modelling for deep penetration problems in clay. Proceedings of 3rd international conference on computational plasticity: fundamentals and applications, 1992. 2:883–94.

[3] van den Berg P. Analysis of soil penetration. PhD thesis, Delft University of Technology, Delft, The Netherlands; 1994.

[4] Yu HS, Herrmann LR, Boulanger RW. Analysis of steady state cone penetration in clay. Journal of Geotechnical and Geoenvironmental Engineering, ASCE 2000; 126(7):594–605.

[5] Lu Q, Randolph MF, Hu Y, Bugarski LC. A numerical study of cone penetration in clay. Geotechnique 2004; 54(4):257–67.

[6] Liyanapathirana, D. S. Arbitrary Lagrangian-Eulerian based finite element analysis of cone penetration in soft clay. Computer and Geotechnics 2009; 36 (5): 851–860.

[7] Nazem, M., Carter J. P., Airey D. W, Chow S. H. Dynamic analysis of a smooth penetrometer free-falling into uniform clay. Geotechnique 2012; 62(10): 893–905.

[8] Randolph, M. F. Characterisation of soft sediments for offshore applications. In Proc. 2nd Int. Conf. on Site Characterisation 2004, volume 1, pages 209–231, Porto.

[9] Skempton, A. W. Residual strength of clays in landslides, folded strata and the labratory. Geotechnique (1985), 35:3–18.

[10] Potts D. M. Numerical analysis: a virtual dream or practical reality? Geotechnique 2003; 53(6):535-572.

[11] Belytschko T, Liu W K, Moran B, Nonlinear Finite Elements for Continua and Structures, Wiley-Blackwell, 2000.

[12] Lanser D., Verwer J.G. Analysis of operator splitting for advection-diffusion-reaction problems from air pollution modelling. Journal of Computational and Applied Mathematics (1999); 111: 201-216.

[13] Hughes T. J. R. and Winget, Finite element rotation effects in numerical integration of rate constitutive equations arising in large-deformation analysis. Journal of the International Journal for Numerical Methods in Engineering 1980, 15:1862-1867.

[14] Duchon J, Splines minimising rotation-invariant semi-norms in Sobolev spaces, Lecture Notes in Mathematics 1977, 57: 85-100.

[15] Wahba G, Spline models for observational data, CBMS-NSF Regional Conference Series in Applied Mathematics, Society for Industrial and Applied Mathematics (SIAM), 1990.

[16] Baguelin F, Frank R, Said YH. Theoretical study of lateral reaction mechanism of pile. Geotechnique 1977; 27(3):405–434.

[17] Vesic, A. S. Expansion of cavities in infinite soil mass. Journal of Soil Mechanics and Foundation Division ASCE 1972; 98(3): 265–290.

[18] van den Berg P. Analysis of soil penetration. PhD thesis, Delft University of Technology, Delft, The Netherlands; 1994.

[19] Lu Q, Randolph MF, Hu Y, Bugarski LC. A numerical study of cone penetration in clay. Geotechnique 2004; 54(4):257–67.

[20] Nazem, M., Carter J. P., Airey D. W, Chow S. H. Dynamic analysis of a smooth penetrometer free-falling into uniform clay. Geotechnique 2012; 62(10): 893–905.

[21] Einav I, Randolph MF. Combining upper bound and strain path methods for evaluating penetration resistance. International Journal for Numerical Methods in Engineering 2005; 63(14):1991–2016.

[22] Osman, A. S. & Randolph, M. F. On the calculation of cumulative strain around full-flow penetrometers in steady-state conditions. International Journal for Numerical and Analytical Methods in Geomechanics (2015). 39(4): 368-387.